JAST, Vol. 5, No. 4, pp 145–159

JAST
Journal of Aerospace Science and Technology

Preload Effect on Nonlinear Dynamic Behavior of Aerodynamic Two-Lobe Journal Bearings

R. Rashidi[1], A. Karami mohammadi[2], F. Bakhtiari nejad[3]

This paper presents the effect of preload on nonlinear dynamic behavior of a rigid rotor supported by two-lobe aerodynamic noncircular journal bearing. A finite element method is employed to solve the Reynolds equation in static and dynamical states and the dynamical equations are solved using Runge-Kutta method. To analyze the behavior of the rotor center in the horizontal and vertical directions under different operating conditions, the dynamic trajectory, the power spectra, the Poincare maps and the bifurcation diagrams are used. From this study, results show how the complex dynamic behavior of this type of system comprising periodic, KT-periodic and quasi-periodic responses of the rotor center varies with changes in preload values by considering two bearing aspect ratios. The results of this study contribute to a better understanding of the nonlinear dynamics of two-lobe aerodynamic noncircular journal bearing system.

NOMENCLATURE

$\bar{C}$	Conventional radial clearance, (m)
$\bar{C}_m$	Minor clearance when rotor and bearing geometric centers are coincident, (m)
$\bar{R}$	Rotor radius, (m)
$\bar{F}_{X0}, \bar{F}_{Y0}$	Components of the fluid film force on the rotor in the steady state, (N)
$\bar{F}_X, \bar{F}_Y$	Components of the fluid film force on the rotor in the dynamical state, (N)
$\bar{W}_0$	Static load, (N)
$\bar{h}$	Film thickness, (m)
$\bar{L}$	Bearing length, (m)
$\bar{m}_r$	Rotor mass, (Kg)
N_i	Shape function
n_e	Number of nodes in an element
n_f	Number of nodes in fluid domain
$\bar{P}^*$	Absolute gas pressure, $(\frac{N}{m^2})$
$\bar{P}$	Partial gas pressure, $(\frac{N}{m^2})$
$\bar{P}_a$	Ambient pressure, $(\frac{N}{m^2})$
$\bar{t}$	Time, (s)
$\bar{U}$	Peripheral speed of the rotor in dynamical state, $(\frac{m}{s})$
$\bar{X}, \bar{Y}$	Cartesian axes with origin at the bearing geometric center, (m)
$\bar{X}_{j0}, \bar{Y}_{j0}$	Coordinates of the rotor center in steady state, (m)
$\bar{X}_j, \bar{Y}_j$	Coordinates of the rotor center in dynamical state, (m)
$\bar{x}, \bar{y}$	Perturbation coordinates of the rotor center measured from its static equilibrium position, (m)
V_x, V_y	Dimensionless velocity of the rotor center in horizontal and vertical directions
A_x, A_y	Dimensionless acceleration of the rotor center in horizontal and vertical directions
δ	Preload in the bearing, $(\frac{\bar{C}_m}{\bar{C}})$
λ	Bearing aspect ratio, $(\frac{\bar{L}}{\bar{D}})$

1. *Ph.D. Candidate, Dept. of Mech. Eng., Shahrood Univ. of Tech., Shahrood, Iran, Email: rrashidim@gmail.com*
2. *Assistant Professor, Dept. of Mech. Eng., Shahrood Univ. of Tech., Shahrood, Iran*
3. *Professor, Dept. of Mech. Eng., Amirkabir Univ.of Tech., Tehran, Iran.*

Λ	Bearing number
$\bar{\mu}$	Ambient dynamic viscosity of the lubricant, $(\frac{N.s}{m^2})$
θ	Angular coordinate measured from X – axis
θ_0^k	Angle of lobe line of centers
θ_1^k, θ_2^k	Angles at the leading and trailing edge of the lobe
$\bar{\omega}$	Rotational speed of the rotor, $(\frac{rad}{s})$
$\bar{\rho}$	Mass eccentricity of the rotor, (m)
τ	Dimensionless time
$\bar{\xi}$	Coordinate along bearing axis measured from mid span, (m)

Superscripts

e	Element numbers
k	Lobe designation

Subscripts

0	Static equilibrium position of the rotor bearing at $\tau = 0$
j	Iteration number

INTRODUCTION

During the past few decades, aerodynamic bearings have received great attention from practical and analytical tribologists. The rapid growth of gas bearing technology is mainly due to its wide range of engineering application such as precision machine tools, high speed aircraft, nuclear reactors, textile spindles, dental drills, *etc.* Aerodynamic journal bearings have the advantage of negligible friction, cleanliness and easy availability of air as the lubricant; however, poor dynamic stability due to low viscosity is a major problem. Therefore, investigation of dynamical behavior is necessary to avoid settling the system in a region whose control is severe.

In 1961, Castelli and Elrod [1] made a significant contribution towards a better understanding of the complex fluid dynamic phenomenon in gas lubrication. These authors presented their assessment of the validity of the assumptions and in the analysis of earlier investigators. They neglected the pressure time derivative term in the Reynolds equation, and obtained the rotor center orbits for a specified set of operating and initial conditions by numerical integration of the equations of motion of the rotor.

Ausman [2] solved the linearized Reynolds equation of self acting bearings to investigate the stability of the static equilibrium position of the rotor. In 1978, Holmes *et.al.* [3] discussed aperiodic behavior in short journal bearings. They noted that moderate level of unbalance and high eccentricity ratio led to an aperiodic response of the shaft at speeds above a critical threshold value. Chandra *et.al.* [4] studied static and dynamic characteristics of four gas lubricated multi-lobe journal bearing configurations. In their work, linearized Reynolds equation was solved by finite element method and comparative stability of four gas-lubricated noncircular journal bearing configurations was done. In 1994, Zhao *et.al.* [5] investigated nonlinear dynamic behavior of an eccentric squeeze film damper-mounted rigid rotor system. The authors showed that for large values of unbalance and static misalignment, the sub-harmonic and quasi-periodic motions generated at speeds of more than twice the system critical speed were bifurcated from the unbalance harmonic solution.

Nonlinear dynamic behavior such as sub-harmonic, quasi-periodic and chaotic motions for suitable values of system parameters in a rigid rotor supported by short bearings were reported by Adiletta *et.al.* through the theoretical and experimental investigations [6-8]. Czolczynski and Kapitaniak [9] described a method which allows control of the Hopf bifurcation of a rotor system supported by two gas bearings. They showed that the damage caused by the growing amplitude of self-excited vibrations can be avoided by proper selection of stiffness and damping coefficients of the air ring.

Nonlinear dynamic and bifurcation analysis of a rigid rotor [10] and a flexible rotor [11] supported by self-acting gas journal bearing were studied by Wang *et.al.*. In both works, by considering rotor mass and rotational speed as the parameters of system, periodic and sub-harmonic motions of the rotor center were reported. In 2005, Wang Jiun-Shen and Wang Cheng-Chi [12] presented bifurcation of a rigid rotor by relative short aerodynamic journal bearings. They discussed how the existence of a complex dynamic behavior comprises periodic and sub-harmonic responses of the rotor center. Also, Wang [13] provided a further understanding of a rigid rotor supported by a relatively short externally pressurized porous gas journal bearing and showed the dynamic behavior of the system with respect to rotor mass and bearing number.

In 2007, Wang *et.al.* studied the behavior of a rigid rotor [14] and a flexible rotor [15] supported by a herringbone-grooved gas journal bearing system. Also, Wang provided a further understanding of a flexible rotor supported by a relatively short herringbone-grooved gas journal bearing system [16]. Their analysis revealed a complex dynamic behavior comprising periodic and quasi-periodic responses of the system.

In references [10-16], a finite difference method with a successive over-relation method was employed

to solve the Reynolds equation. In later studies, Wang and Yau [17] and Wang [18] used a hybrid numerical method combining the differential transformation method and the finite difference method to study the nonlinear dynamic behavior of a rigid rotor and a flexible rotor supported by a spherical gas-lubricated bearing system, respectively.

Rahmatabadi and Rashidi investigated static and dynamic characteristics of noncircular gas-lubricated journal bearings by considering the effect of mount angle [19] and preload [20]. They showed noncircular bearings have better dynamic characteristics than circular bearings. Also, by using a suitable value for the mount angle, stability margin can be increased.

Although previous works provide insight into the behavior of the system, the bifurcation and nonlinear dynamic behavior of the gas film in an aerodynamic noncircular journal bearing has not been examined. Therefore, this paper presents the effect of preload on nonlinear dynamic behavior of a rigid rotor supported by two-lobe noncircular aerodynamic journal bearing (Figure 1).

The amount of preload of a noncircular bearing determines its noncircularity or ellipticity relative to a plane journal bearing. For zero preload, the rotor touches the lobes at their line of centers whereas with unit preload, a lobed bearing reduces into an axial groove plane journal bearing [20].

Due to the nonlinearity of the gas film pressure, it is very difficult to solve the Reynolds equation analytically. Therefore, finite element methods have been employed to obtain the solution, and then Runge-Kutta method has been subsequently used to solve this equation and equations of motion simultaneously to obtain position, velocity and acceleration of the rotor center.

MATHEMATICAL ANALYSIS

Governing equations

The geometric details of a two-lobe noncircular bearing configuration are shown in Figure 1. Analysis of aerodynamic noncircular bearing involves solution of the governing equations separately for an individual lobe of the bearing, treating each lobe as an independent partial bearing. To generalize the analysis for all noncircular geometries, the film geometry of each lobe is described with reference to bearing fixed Cartesian axes (Figure 1). Thus, the film thickness in the clearance space of the kth lobe, with the rotor in a dynamical state is expressed as [4]:

$$\bar{h} = \bar{C} - (\bar{X}_j)\cos\theta - (\bar{Y}_j)\sin\theta + (\bar{C} - \bar{C}_m)\cos(\theta - \theta_0^k) \tag{1}$$

where $(\bar{X}_j, \bar{Y}_j)$ is the rotor center coordinate in the dynamical state and θ_0^k is angle of lobe line of centers.

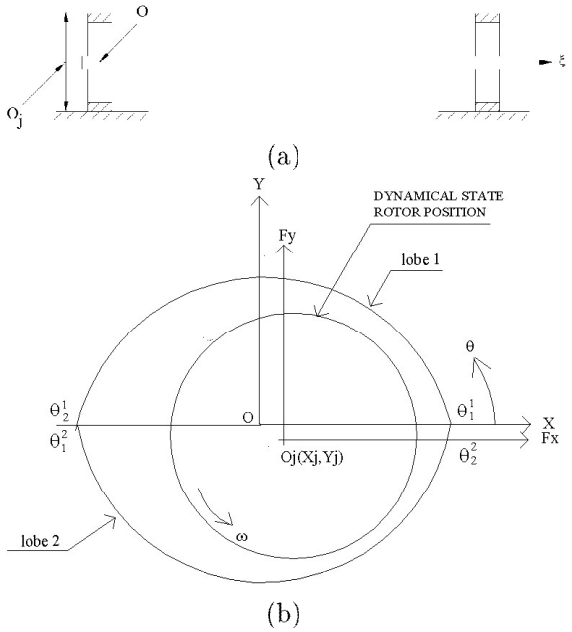

Figure 1. (a) Model of a rigid rotor supported by two aerodynamic noncircular journal bearings and (b) geometric model of two-lobe noncircular bearing.

$\bar{C}$ and $\bar{C}_m$ are conventional radial clearance and minor clearance, when journal and bearing geometric centers are coincident. The pressure governing equation of isothermal flow field in a bearing lobe is modeled by the Reynolds equation as follows [11]:

$$\frac{\partial}{\partial \bar{X}}\left\{\bar{h}^3\bar{P}^*\frac{\partial \bar{P}^*}{\partial \bar{X}}\right\} + \frac{\partial}{\partial \bar{Y}}\left\{\bar{h}^3\bar{P}^*\frac{\partial \bar{P}^*}{\partial \bar{Y}}\right\} = 6\bar{\mu}\left[\bar{U}\frac{\partial}{\partial \bar{X}} + 2\frac{\partial}{\partial \bar{t}}\right](\bar{P}^*\bar{h}) \tag{2}$$

in which $\bar{P}^*$ is the absolute gas pressure, $\bar{\mu}$ is the gas viscosity, $\bar{U}$ is the peripheral speed of the rotor and $\bar{t}$ is the time.

It will be more convenient to express $\bar{P}^*$ as:

$$\bar{P}^* = \bar{P}_a + \bar{P} \tag{3}$$

where $\bar{P}_a$ and $\bar{P}$ are the ambient and partial pressure, respectively.

In order to nondimensionalize Eqs. (1) and (2), let:

$$\bar{C}_m = \bar{C}\delta,\ (\bar{X}_j, \bar{Y}_j) = \bar{C}_m(X_j, Y_j),\ \bar{X} = \bar{R}\theta,\ \bar{Y} = \bar{R}\xi,$$

$$\bar{h} = \bar{C}_m h,\quad \bar{P} = \bar{P}_a P,\quad \bar{U} = \bar{U}_0 U = \bar{R}\bar{\omega}_0 U,\quad \bar{t} = \frac{\tau}{\bar{\omega}_0}$$

where $\bar{\omega}_0$ is the rotational speed in the steady state, and $\bar{R}$ is the rotor radius. Substituting these variables in Eq. (1), the nondimensional film thickness can be obtained as:

$$h = \frac{1}{\delta} - (X_j)\cos\theta - (Y_j)\sin\theta + (\frac{1}{\delta} - 1)\cos(\theta - \theta_0^k) \tag{4}$$

and by substituting Eq. (3) in Eq. (2) and simplifying it, the Reynolds equation in nondimensional form can be expressed as:

$$\frac{\partial}{\partial\theta}\left\{h^3(P+1)\frac{\partial P}{\partial\theta}\right\}+\frac{\partial}{\partial\xi}\left\{h^3(P+1)\frac{\partial P}{\partial\xi}\right\}=\Lambda\left[U\frac{\partial}{\partial\theta}+2\frac{\partial}{\partial\tau}\right]\{(P+1)h\} \tag{5}$$

where θ and ξ are the coordinates in the circumferential and axial directions, respectively and:

$$\Lambda=\frac{6\bar{\mu}\bar{\omega}_0\bar{R}^2}{\bar{P}_a\bar{C}_m^2}$$

is the dimensionless parameter called the compressibility number or bearing number.

The Reynolds equation is a nonlinear partial differential equation; therefore, it can be solved using finite element method. For this purpose, let the function variable:

$$\Psi=\Psi(\tau)=Ph$$

be introduced into Eq. (5), which then becomes:

$$\frac{\partial}{\partial\theta}\left\{h(\Psi+h)\frac{\partial\Psi}{\partial\theta}-(\Psi+h)\Psi\frac{\partial h}{\partial\theta}\right\}+\frac{\partial}{\partial\xi}\left\{h(\Psi+h)\frac{\partial\Psi}{\partial\xi}\right\}=\Lambda\left(U\frac{\partial}{\partial\theta}+2\frac{\partial}{\partial\tau}\right)(\Psi+h) \tag{6}$$

For the finite element formulation, the Galerkin's weighted residual of Eq. (6) for an element of the discretized space domain of Ψ field is written as:

$$\iint_{A^e}\left[\frac{\partial\Psi^e}{\partial t}-\frac{1}{2\Lambda}\frac{\partial}{\partial\theta}\left\{h(\Psi^e+h)\frac{\partial\Psi^e}{\partial\theta}-(\Psi^e+h)\Psi^e\frac{\partial h}{\partial\theta}\right\}-\frac{1}{2\Lambda}\frac{\partial}{\partial\xi}\left\{h(\Psi^e+h)\frac{\partial\Psi^e}{\partial\xi}\right\}+\frac{1}{2}U\frac{\partial}{\partial\theta}(\Psi^e+h)+\frac{\partial h}{\partial\tau}\right]N_i^e d\theta d\xi=0 \tag{7}$$

where N_i^e is an approximation function and A^e is the area of the element. By considering the discretized domain of Ψ variable and letting, the Ψ function be approximated as:

$$\Psi^e=\sum_{j=1}^{n_e}N_j^e\Psi_j(\tau) \tag{8}$$

where 'e' refers to an element, n_e is the number of nodes in the element, N_j^e 's are the shape functions and Ψ_j 's are the nodal values of Ψ at time τ. Using Eq. (8) in Eq. (7) and with integral simplifications, the finite element equations for an element of the discretized flow field domain can be obtained as:

$$[F]^e\left\{\dot{\Psi}\right\}^e=\{V\}^e+\{Q\}^e \tag{9}$$

in which the components of the element matrices are:

$$F_{ij}^e=\iint_{A^e}N_i^eN_j^e d\theta d\xi \tag{10a}$$

$$V_i^e=-\frac{1}{2\Lambda}\iint_{A^e}(\Psi^e+h)\left\{h\left(\frac{\partial\Psi^e}{\partial\theta}\frac{\partial N_i^e}{\partial\theta}+\frac{\partial\Psi^e}{\partial\xi}\frac{\partial N_i^e}{\partial\xi}\right)-\left(\Psi^e\frac{\partial h}{\partial\theta}+\Lambda U\right)\frac{\partial N_i^e}{\partial\theta}\right\}d\theta d\xi-\iint_{A^e}\frac{\partial h}{\partial\tau}N_i^e d\theta d\xi \tag{10b}$$

$$Q_i^e=\int_{s^e}(\Psi^e+h)\left\{h\frac{\partial\Psi^e}{\partial\theta}-\Psi^e\frac{\partial h}{\partial\theta}-\Lambda U\right\}N_i^e d\xi+\int_{s^e}(\Psi^e+h)h\frac{\partial\Psi^e}{\partial\xi}N_i^e d\theta \tag{10c}$$

where S^e is the boundary of the element.

The assembly of Eq. (8) for all elements of Ψ domain yields the global equations:

$$[F]_{n_f\times n_f}\left\{\dot{\Psi}\right\}_{n_f\times 1}=\{V\}_{n_f\times 1}+\{Q\}_{n_f\times 1} \tag{11}$$

where n_f is the total number of nodes.

The boundary conditions of the variables for the solution of Eq. (11) are:

$$\Psi(\theta_1^k,\xi,\tau)=\Psi(\theta_2^k,\xi,\tau)=0$$
$$\dot{\Psi}(\theta_1^k,\xi,\tau)=\dot{\Psi}(\theta_2^k,\xi,\tau)=0$$
$$\Psi(\theta,\pm\lambda,\tau)=0$$
$$\dot{\Psi}(\theta,\pm\lambda,\tau)=0 \tag{12}$$

At any instant when kinematic state of the rotor center is known, Eq. (11) comprises two variables, Ψ_i and Q_i to be determined. However, at the internal nodes of the discretized space domain, the flux Q_i is zero and Ψ_i is unknown. At the nodes on the boundaries $\xi=\pm\lambda$, and edges of the lobes (θ_1^k and θ_2^k), Ψ_i is known while Q_i is not known. Thus, Eq. (11) really involves as many unknowns as the number of equations, and may be solved by implementing the boundary conditions. The solution of these equations yields:

$$\left\{\dot{\Psi}\right\}_{n_f\times 1}=\{g\}_{n_f\times 1} \tag{13}$$

where $g_i=g_i(P,\tau)\,;\ \ i=1,2,...,n_f$

Rotor dynamic equations and computation procedure

In the dynamical state, the equations of motion of the rotor can be written as:

$$\bar{m}_r \frac{d^2\bar{x}}{d\bar{t}^2} = \left(\bar{F}_X - \bar{F}_{X0}\right) + \bar{m}_r \bar{\rho}\bar{\omega}^2 \cos\bar{\omega}\bar{t} \tag{14}$$

$$\bar{m}_r \frac{d^2\bar{y}}{d\bar{t}^2} = \left(\bar{F}_Y - \bar{F}_{Y0}\right) + \bar{m}_r \bar{\rho}\bar{\omega}^2 \sin\bar{\omega}\bar{t} \tag{15}$$

where $\bar{m}_r$ is the mass of rotor, $\bar{\rho}$ is the mass eccentricity of the rotor and $\bar{\omega}$ is the rotational speed. $(\bar{x}, \bar{y})$ is the perturbed position of the rotor center defined as:

$$\bar{x} = \bar{X}_j - \bar{X}_{j0}\,,\ \bar{y} = \bar{Y}_j - \bar{Y}_{j0} \tag{16}$$

also, $(\bar{F}_X, \bar{F}_Y)$ and $(\bar{F}_{X0}, \bar{F}_{Y0})$ are the components of fluid film force on the rotor in the dynamical and steady states, respectively.

The components of fluid film force on the rotor are given by:

$$\left\{ \begin{array}{c} \bar{F}_X - \bar{F}_{X_0} \\ \bar{F}_Y - \bar{F}_{Y_0} \end{array} \right\} = -\bar{P}_a \bar{R}^2 \left\{ \begin{array}{c} \cos\theta \\ \sin\theta \end{array} \right\} d\theta d\xi \tag{17}$$

where, A is the pressure area on the rotor, $P_0 = P_0(X_{j0}, Y_{j0})$ and $P = P(X, Y, V_x, V_y, \tau)$ are the film pressures in the steady state and in the dynamical state, respectively.

The following transformation is introduced:

$$x = \bar{x}/\bar{C}_m, y = \bar{y}/\bar{C}_m$$

and defining nondimensional groups, we have:

$$F_X = \frac{\bar{F}_X}{\bar{P}_a\bar{R}^2},\ F_{X_0} = \frac{\bar{F}_{X_0}}{\bar{P}_a\bar{R}^2},\ F_Y = \frac{\bar{F}_Y}{\bar{P}_a\bar{R}^2},$$

$$F_{Y_0} = \frac{\bar{F}_{Y_0}}{\bar{P}_a\bar{R}^2},\ m_r = \frac{\bar{m}_r\bar{C}_m\bar{\omega}^2}{\bar{P}_a\bar{R}^2},\ \rho = \frac{\bar{m}_r\bar{\rho}\bar{\omega}^2}{\bar{P}_a\bar{R}^2}$$

substituting these nondimensional groups into Eqs. (14-15) yields:

$$A_x = \frac{d^2x}{d\tau^2} = \frac{F_X - F_{X0}}{m_r} + \frac{\rho}{m_r}\cos\tau \tag{18}$$

$$A_y = \frac{d^2y}{d\tau^2} = \frac{F_Y - F_{Y0}}{m_r} + \frac{\rho}{m_r}\sin\tau \tag{19}$$

By defining the state variables:

$$S_1 = x,\ S_2 = y,\ S_3 = V_x,\ S_4 = V_y \tag{20}$$

the equations of motion are transformed into the following state space equations:

$$\frac{dS_1}{d\tau} = S_3 \tag{21}$$

$$\frac{dS_2}{d\tau} = S_4 \tag{22}$$

$$\frac{dS_3}{d\tau} = \frac{F_X - F_{X0}}{m_r} + \frac{\rho}{m_r}\cos\tau \tag{23}$$

$$\frac{dS_4}{d\tau} = \frac{F_Y - F_{Y0}}{m_r} + \frac{\rho}{m_r}\sin\tau \tag{24}$$

Equations (13) and (21-24) describe a nonlinear dynamic system. The equations are restated for convenience:

$$\begin{aligned} \frac{dS_i}{d\tau} &= f_i\left(P, S_1, S_2S_3, S_4, \tau\right) \quad i = 1,2,3,4 \\ \frac{d\Psi_i}{d\tau} &= g_i\left(P, S_1, S_2S_3, S_4, \tau\right) \quad i = 1,2,...,n_f \end{aligned} \tag{25}$$

The solution procedure commences with an initial static equilibrium state, and initial conditions are selected from the static model. Therefore, at the beginning, Reynolds equation should be solved in the steady state to obtain Ψ_0 and (X_{j0}, Y_{j0}). Meanwhile, the initial velocity of the rotor is assumed to be zero. The numerical integration of Eq. (25) is carried out by the fourth order Runge-Kutta method. By this method, acceleration, velocity and displacement of the rotor are estimated at each time step, and are utilized for initial conditions in the next time step. Then, the displacement of the rotor center obtained from each step is used to update the film thickness and the new pressure distribution can be obtained to yield the new dynamical force by integrating it.

NUMERICAL STUDIES

Due to the high nonlinearity of gas film forces, the system behavior is studied numerically using the finite element method. The flow domain of each lobe of two-lobe noncircular bearing is rectangular, therefore, four-noded rectangular isoparametric element is employed to mesh flow field. In this study, the fourth order Runge-Kutta method is used for the integration of Eq. (25). By many trails, time interval of $\Delta t = \pi/300$ is found to be the optimal considering accuracy of the results and computation time.

The Gauss-Siedel iteration method is employed for the solution of Eq. (11) to obtain $\left\{\dot{\Psi}\right\}$ column during the time integral scheme. The convergence criterion is applied on every nodal value $\dot{\Psi}_i$ as:

$$\left|\dot{\Psi}_{i,j+1} - \dot{\Psi}_{i,j}\right| < \dot{\Psi}_{tol} \qquad i = 1,2,...n_f \tag{26}$$

where j is the iteration number. This condition states that no nodal values of $\dot{\Psi}$ in the solution field should change by an amount greater than $\dot{\Psi}_{tol}$ as a result of

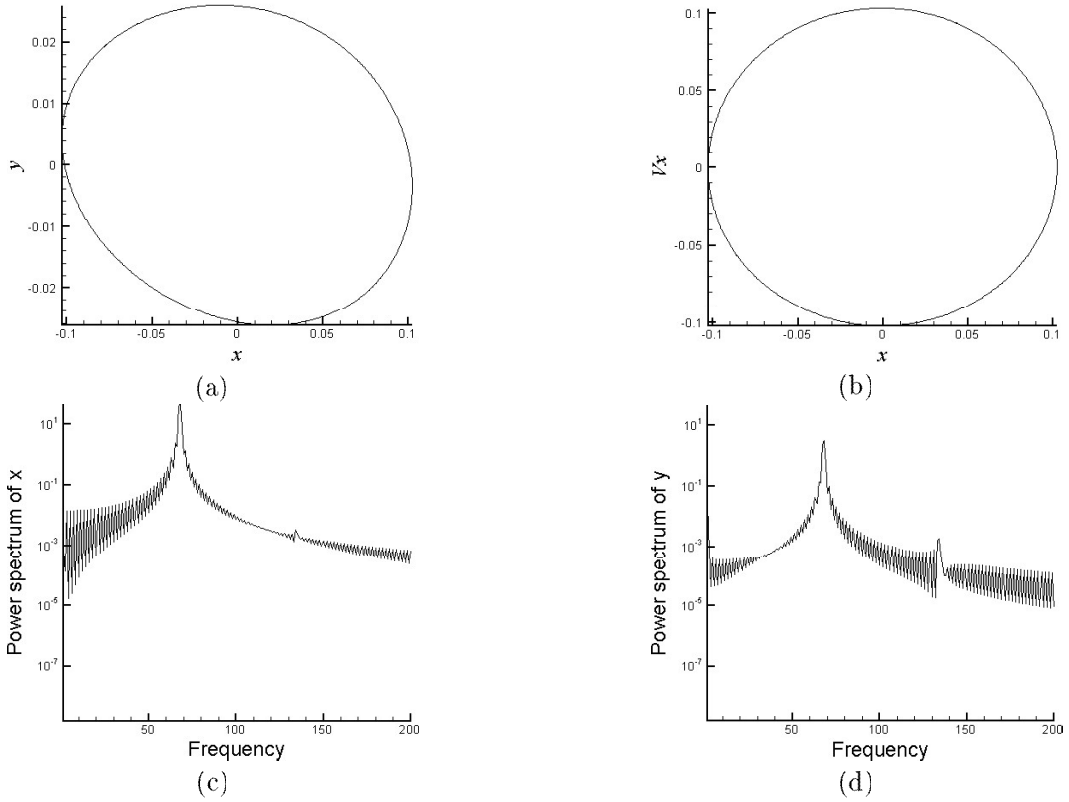

Figure 2. Trajectory of the rotor center at $\delta = 0.42$ (a); phase portraits of rotor center (b) and power spectra of rotor displacement in horizontal (c) and vertical (d) directions for $\lambda = 1$.

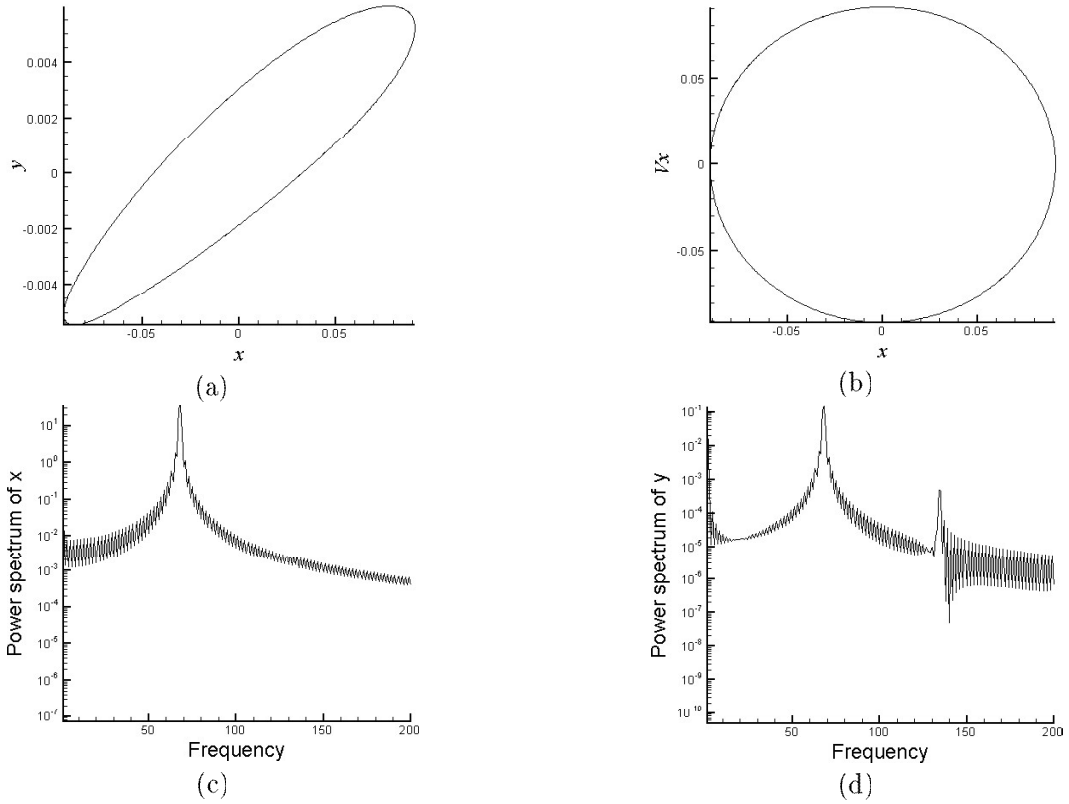

Figure 3. Trajectory of the rotor center at $\delta = 0.48$ (a); phase portraits of rotor center (b) and power spectra of rotor displacement in horizontal (c) and vertical (d) directions for $\lambda = 1$

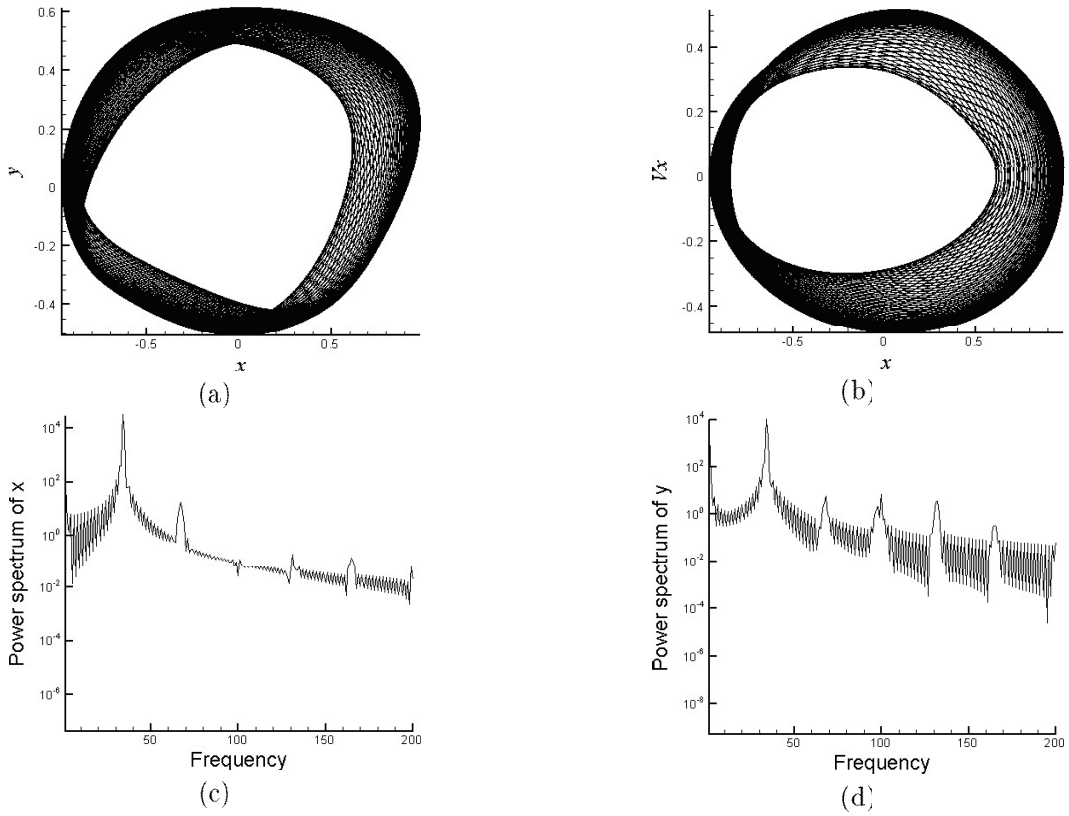

Figure 4. Trajectory of the rotor center at $\delta = 0.516$ (a); phase portraits of rotor center (b) and power spectra of rotor displacement in horizontal (c) and vertical (d) directions for $\lambda = 1$

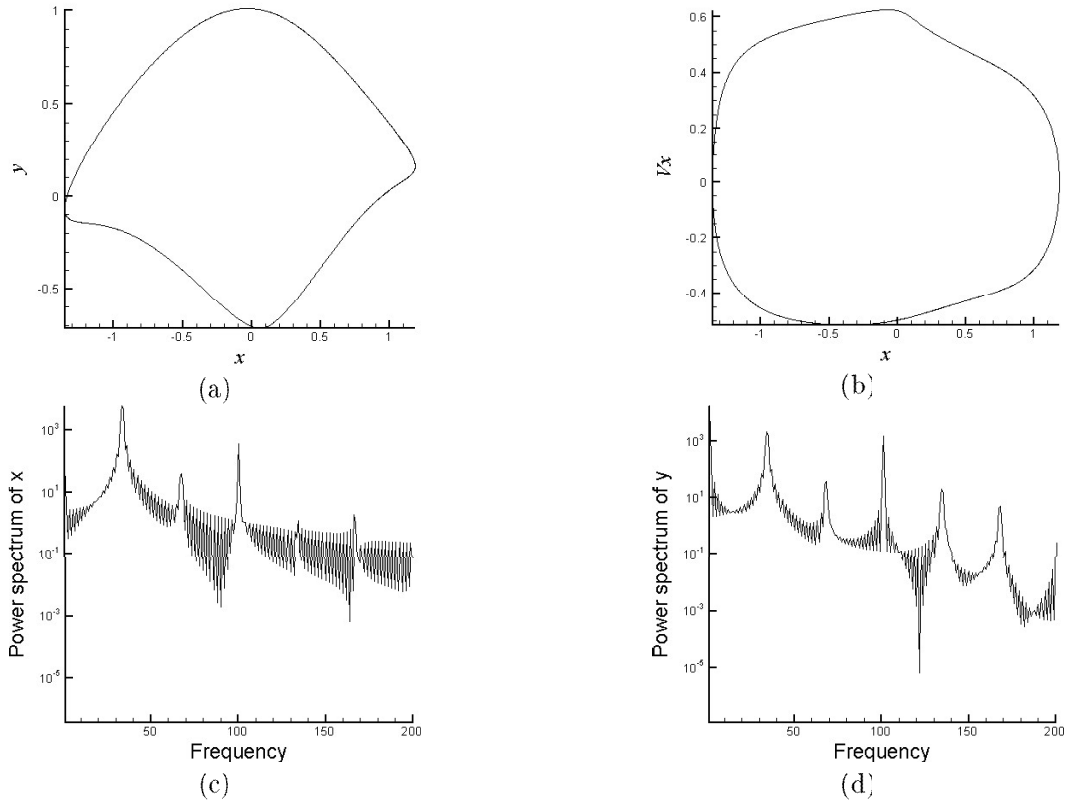

Figure 5. Trajectory of the rotor center at $\delta = 0.548$ (a); phase portraits of rotor center (b) and power spectra of rotor displacement in horizontal (c) and vertical (d) directions for $\lambda = 1$

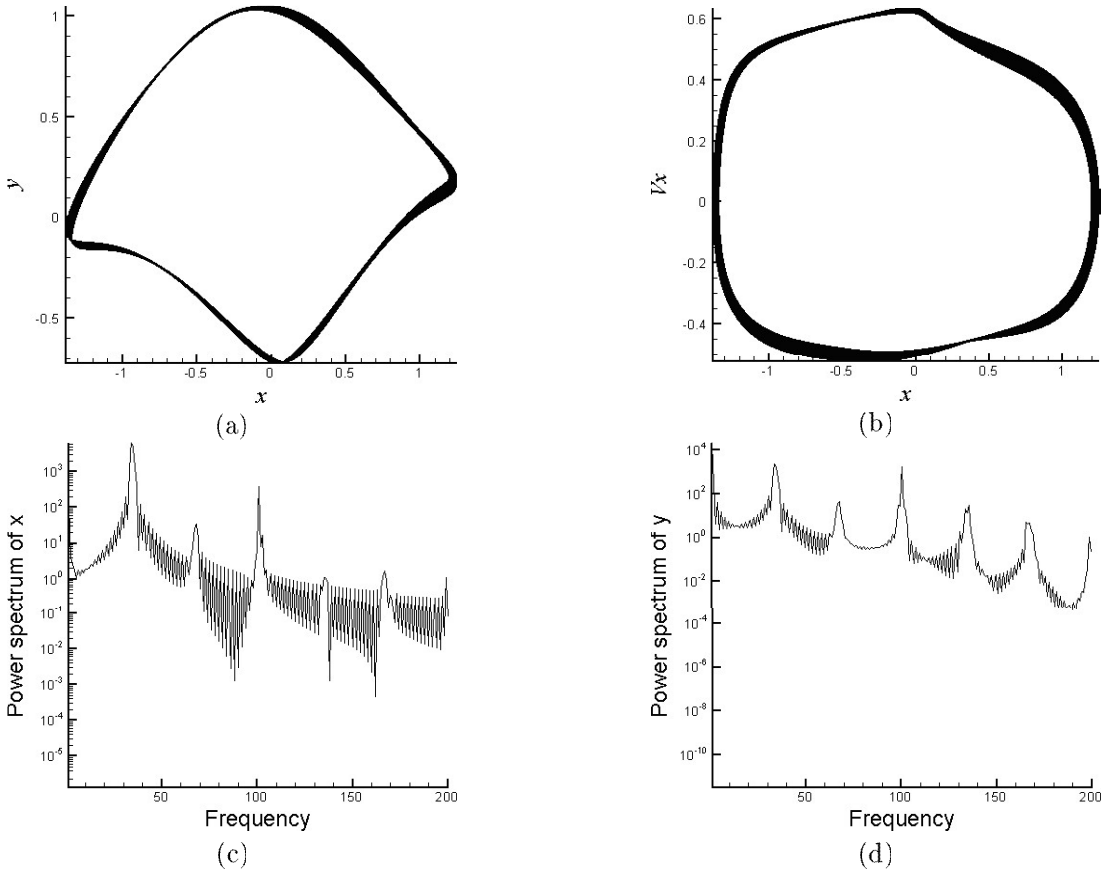

Figure 6. Trajectory of the rotor center at $\delta = 0.554$ (a); phase portraits of rotor center (b) and power spectra of rotor displacement in horizontal (c) and vertical (d) directions for $\lambda = 1$

one Gauss-Siedel iteration. In the present work $\dot{\Psi}_{tol}$ is taken to be 10^{-6}.

The time series data of the first 600000 time steps are excluded from dynamic behavior investigation to ensure that the data used represent steady state conditions. The resulting data include the orbital paths of the rotor center. These data are then used to generate the power spectra, Poincare maps and bifurcation diagrams.

Fast Fourier transformation is used to obtained power spectra of the rotor center in horizontal and vertical directions.

To generate Poincare map, a Poincare section that is transverse to the flow of a given dynamic system is considered. A point on this section is a return point of the time series at the constant time interval of T, where T is the driven period of the exciting force in non-autonomous systems. The projection of a Poincare section on the $x-y$ plane is related to the Poincare map of the dynamic system. Bifurcation diagram is a useful means to observe the nonlinear dynamic behavior of a system. To draw a bifurcation diagram, an obtained point on the Poincare map is used with varying preload values by a constant step.

RESULTS AND DISCUSSION

In this paper the detailed data are as follows [10-11]:

$$\bar{C} = 3 \times 10^{-5} m, \quad \bar{R} = 0.05\, m,$$

$$\bar{\mu} = 1.8 \times 10^{-5} \frac{Kg}{m.s}, \quad \bar{P}_a = 1.013 \times 10^5 \frac{N}{m^2}$$

Also, the mass eccentricity of the rotor is $\bar{\rho} = 0.001\, mm$. Two-lobe noncircular gas bearing is loaded by considering a bearing number of $\Lambda = 25$; the static load is taken to be $\bar{W}_0 = 506.5\, N$, and mass of the rotor is specified to be $\bar{m}_r = 25.82\, Kg$.

To be sure of the proper working of the prepared algorithm, validation of our results has been done in the following manner:

Finite difference method has been applied to solving Reynolds equation, and instead of using Runge-Kutta method, direct method discussed in Refs. [10-15] has been used to obtain acceleration, velocity and displacement of the rotor center. Table 1 shows the results obtained from the time series data for a two-lobe bearing through two methods, where static load and mass of the rotor are chosen to be $\bar{W}_0 = 506.5\, N$ and $\bar{m}_r = 25.8\, Kg$, respectively. Also, the bearing number

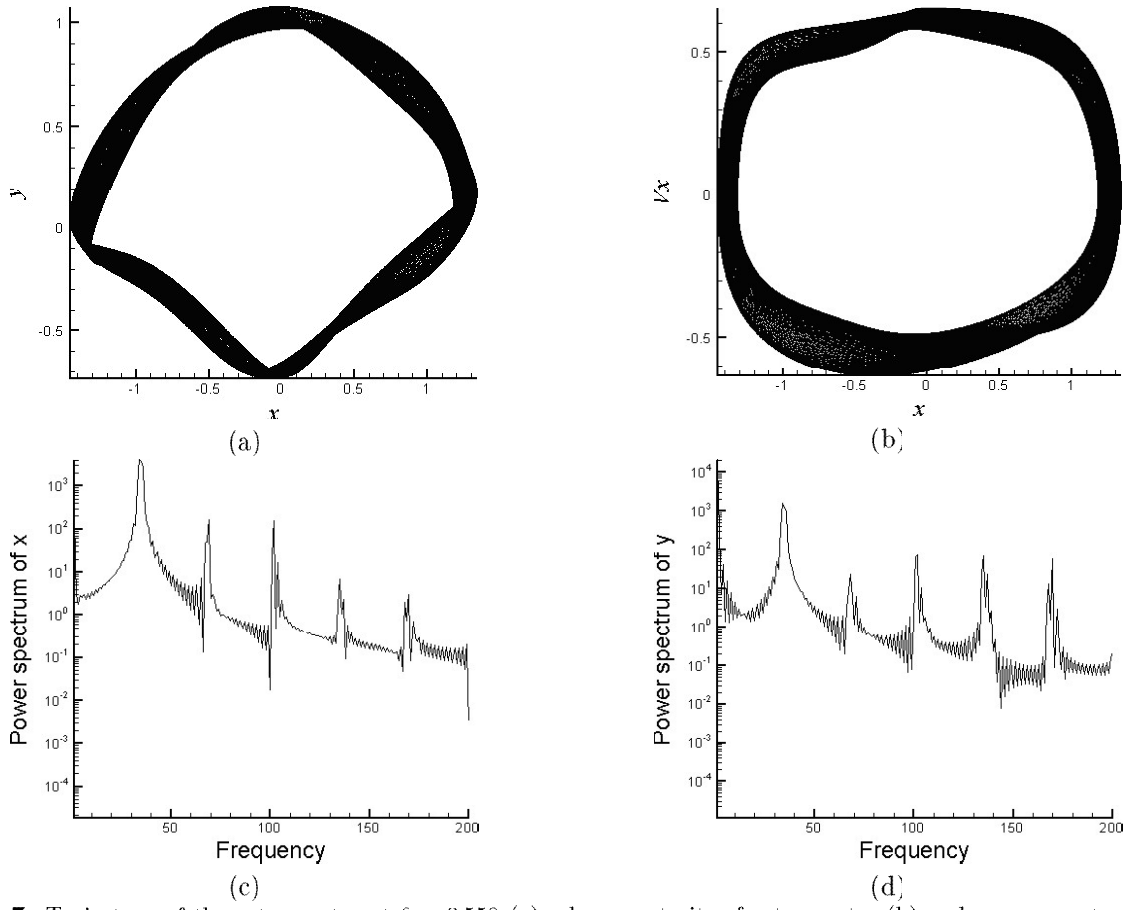

Figure 7. Trajectory of the rotor center at $\delta = 0.558$ (a); phase portraits of rotor center (b) and power spectra of rotor displacement in horizontal (c) and vertical (d) directions for $\lambda = 1$

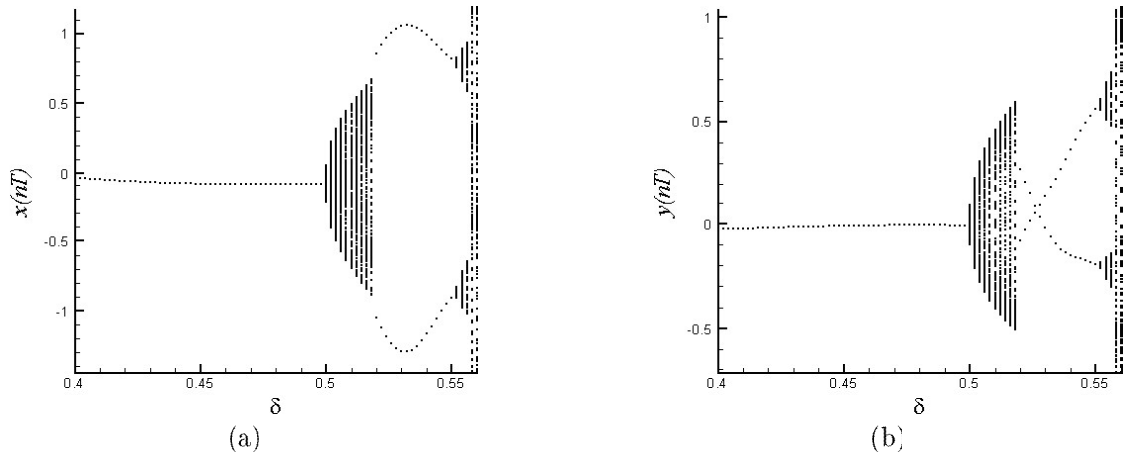

Figure 8. Bifurcation diagrams: (a) $x(nT)$ and (b) $y(nT)$ versus preload for $\lambda = 1$.

Table 1. Comparison of the results in the dynamical state calculated by two methods for a two-lobe bearing.

Preload	Methods	x			y		
		$\tau = 10$	$\tau = 100$	$\tau = 1000$	$\tau = 10$	$\tau = 100$	$\tau = 1000$
0.4	FEM	-0.041972	-0.036867	0.062038	0.025430	-0.019359	-0.015659
	FDM	-0.041974	-0.035860	0.061688	0.024744	-0.019265	-0.015123
0.5	FEM	0.070029	-0.087053	0.002880	0.012823	-0.004511	-0.013407
	FDM	0.068351	-0.086471	0.003743	0.013035	-0.004903	-0.013310

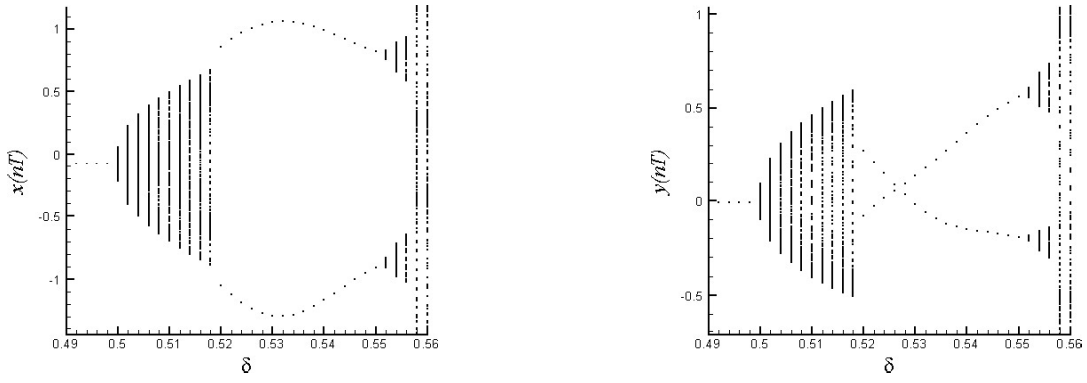

Figure 9. Local bifurcation diagrams of (a) $x(nT)$ and (b) $y(nT)$ versus preload ($0.49 \leq \delta \leq 0.56$) for $\lambda = 1$.

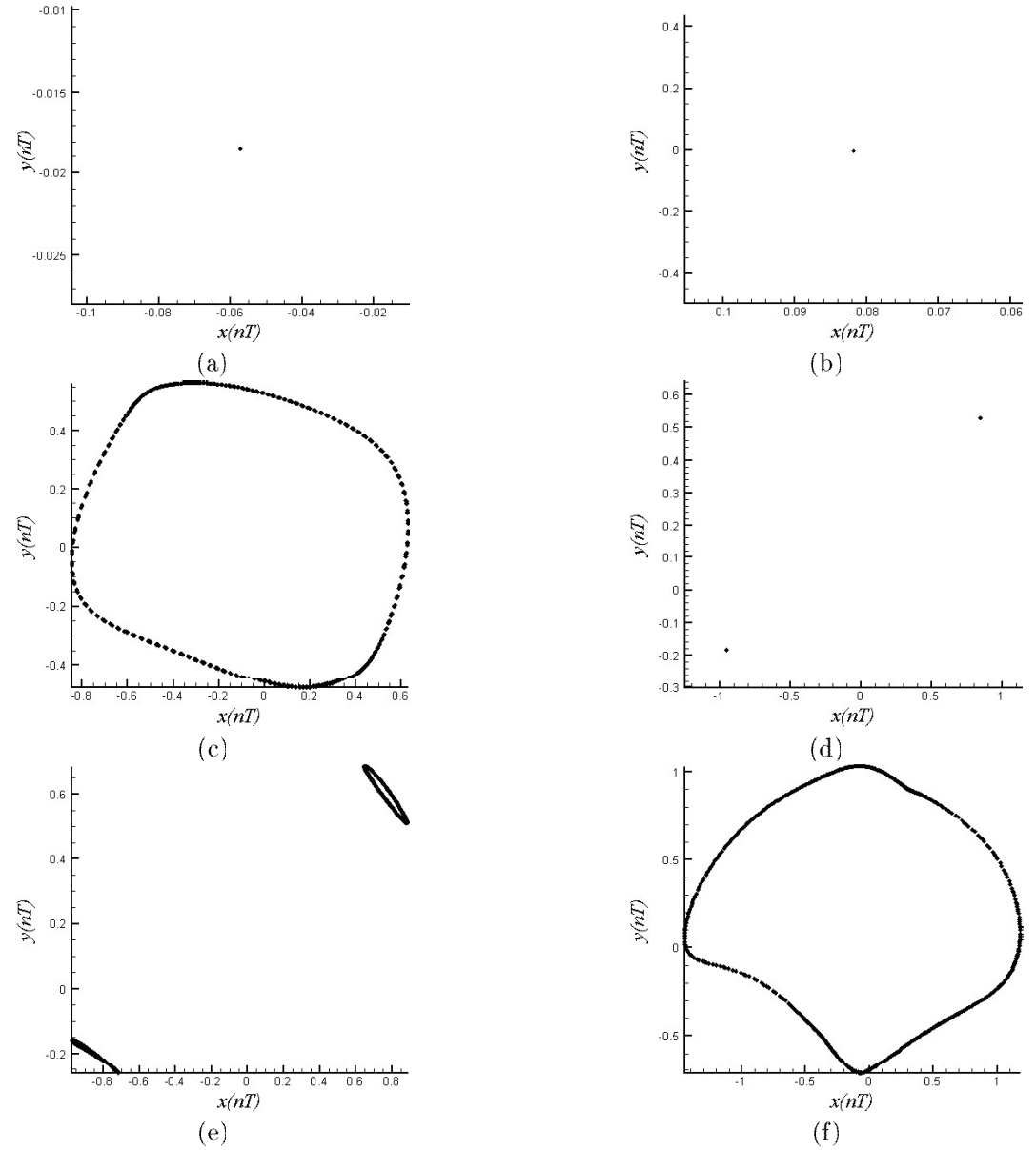

Figure 10. Poincare maps of the rotor center trajectory at (a) $\delta = 0.42$, (b) 0.48, (c) 0.516, (d) 0.548, (e) 0.554, (f) 0.558.

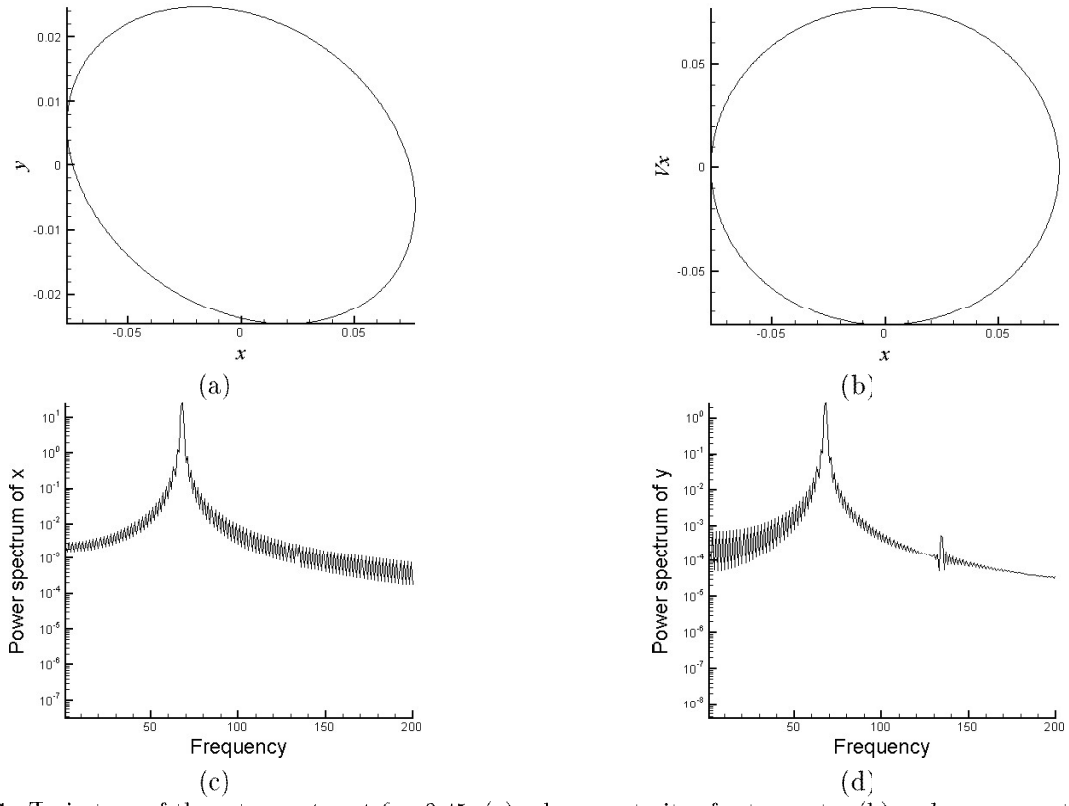

Figure 11. Trajectory of the rotor center at $\delta = 0.45$, (a); phase portraits of rotor center (b) and power spectra of rotor displacement in horizontal (c) and vertical (d) directions for $\lambda = 1.5$.

is taken to be $\Lambda = 25$. It is observed that the results of these two methods are very close.

Case 1

In the first case, the bearing aspect ratio is taken to be $\lambda = 1$ and its results are as follows:

Figures 2(a), 3(a),... , 7(a) show the rotor center orbits at different values of the preload. Regular motion is shown at $\delta = 0.42$ and 0.48. But, regular motion loses its stability and becomes irregular when the preload is increased to $\delta = 0.516$. Regular motion can be seen at $\delta = 0.548$ again. By increasing the preload value, irregular motion appears at $\delta = 0.554$, and 0.558. This condition persists for all preload values in the range 0.554 – 0.56.

From Figures 2(b), 3(b), ..., 7(b) it is observed that the phase portraits of the rotor center are regular at $\delta = 0.42$ and 0.48 and they then become irregular at $\delta = 0.516$. It can also be seen that the phase portraits of the rotor center are regular at $\delta = 0.548$, but become irregular at $\delta = 0.554$ and 0.558.

Figures 2(c,d), 3(c,d), ..., 7(c,d) show the dynamic responses of the rotor center in horizontal and vertical directions. It is found that the frequency responses of the rotor center demonstrate a harmonic motion for the preload values $\delta = 0.42$ and 0.48 in both directions. The frequency responses of the rotor center become quasi-periodic motion at $\delta = 0.516$. But, they become KT-periodic motion at $\delta = 0.548$. By increasing the preload value to $\delta = 0.554$, the frequency responses of the rotor center become quasi-periodic, and this behavior persists at $\delta = 0.558$.

By considering the preload value as a parameter of system, qualitatively different behavior can be observed in Figure 8 at the range of $0.4 \leq \delta \leq 0.56$. Local bifurcation of the rotor center in the preload range of $0.49 \leq \delta \leq 0.56$ is shown in Figure 9. Results show that, before $\delta = 0.5$, the system has a periodic motion in the horizontal and vertical directions. Figures 10(a) and (b) show the Poincare maps at $\delta = 0.42$ and 0.48, respectively. One point on these maps confirms T -periodic motion of the rotor in both displacements. It can be seen that quasi-periodic motion occurs in the interval of $0.5 \leq \delta \leq 0.518$. The Poincare map at $\delta = 0.516$ is shown in Figure 10(c) and closed curve formed on this map demonstrates quasi-periodic motion of the rotor center at $\delta = 0.516$. $2T$ -periodic motion occurs in the interval of $0.518 < \delta < 0.552$ and two discrete points in Figure 10(d) confirms this behavior at $\delta = 0.548$. The system is irregular in the range of $0.552 \leq \delta \leq 0.56$ and closed curved is shown in Figures 10(e) and (f) demonstrate quasi-periodic

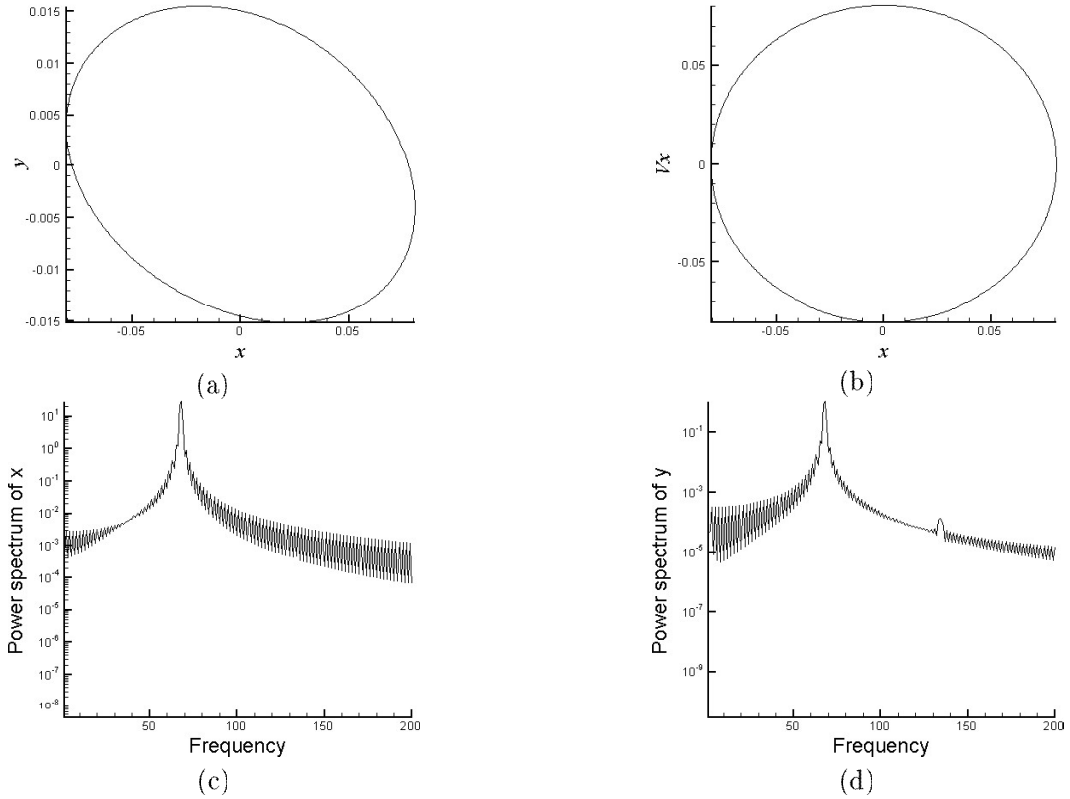

Figure 12. Trajectory of the rotor center at $\delta = 0.5$, (a); phase portraits of rotor center (b) and power spectra of rotor displacement in horizontal (c) and vertical (d) directions for $\lambda = 1.5$.

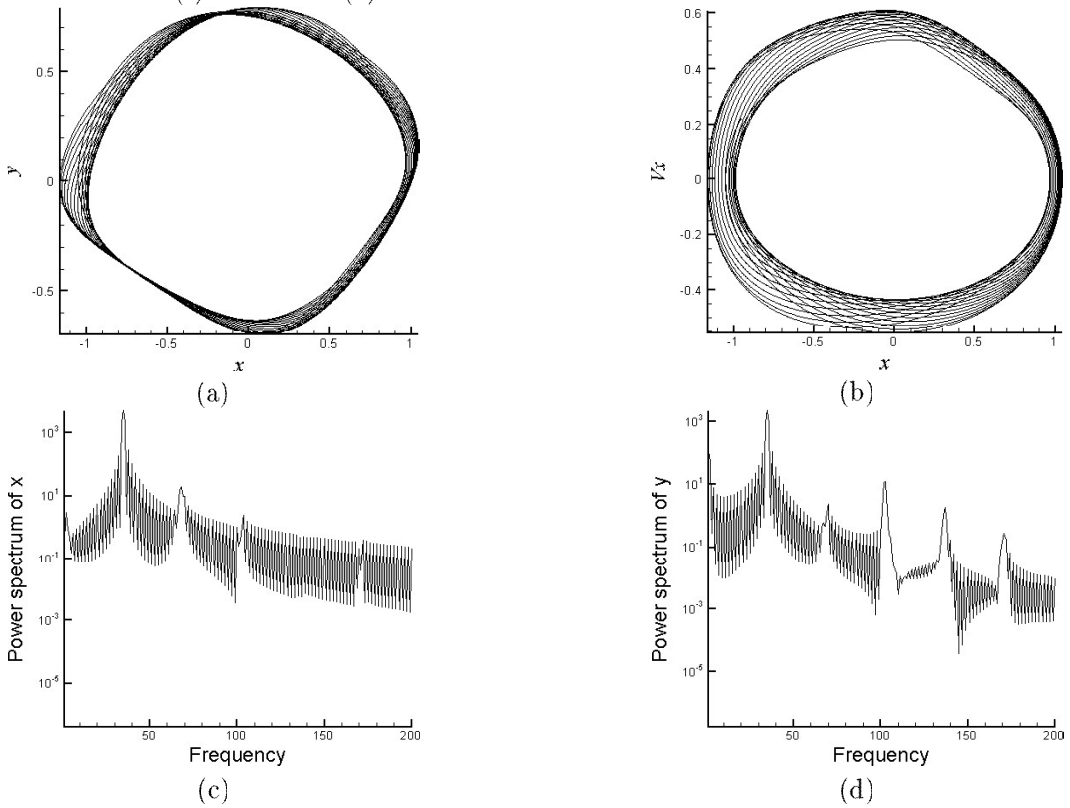

Figure 13. Trajectory of the rotor center at $\delta = 0.55$, (a); phase portraits of rotor center (b) and power spectra of rotor displacement in horizontal (c) and vertical (d) directions for $\lambda = 1.5$.

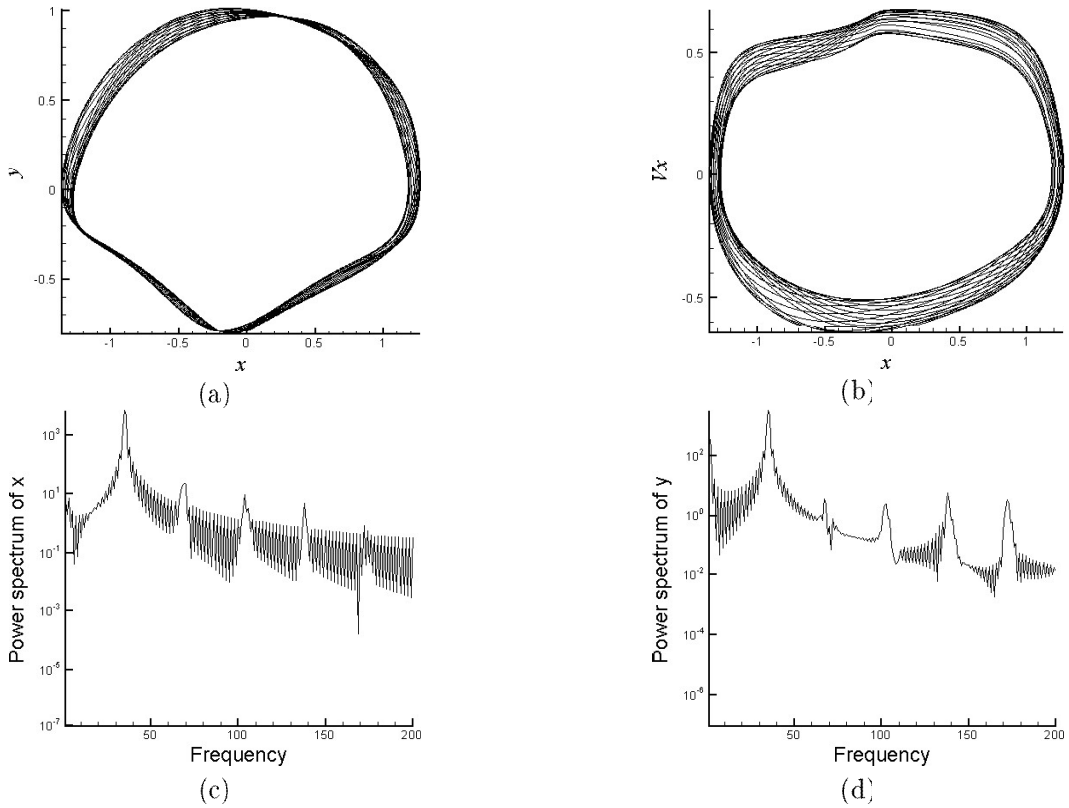

Figure 14. Trajectory of the rotor center at $\delta = 0.6$ (a); phase portraits of rotor center (b) and power spectra of rotor displacement in horizontal (c) and vertical (d) directions for $\lambda = 1.5$

motion at $\delta = 0.554$ and 0.558, respectively. When preload value exceeds $\delta = 0.56$ contact between rotor and bearing would occur.

Case 2

In the second case, the bearing aspect ratio is taken to be $\lambda = 1.5$, and its results are as follows:

Figures 11(a), 12(a), 13(a) and 14(a) show the rotor center orbits at different values of the preload. Regular motion is shown at $\delta = 0.45$ and 0.5. But, regular motion loses its stability and becomes irregular when the preload values are increased to $\delta = 0.55$ and 0.6.

From Figures 11(b), 12(b), 13(b) and 14(b) it is observed that the phase portraits of the rotor center are regular at $\delta = 0.45$ and 0.5 then they become irregular at $\delta = 0.55$ and 0.6.

Figures 11(c,d), 12(c,d), 13(c,d) and 14(c,d) show the dynamic responses of the rotor center in horizontal and vertical directions. It is found that the frequency responses of the rotor center demonstrate a harmonic motion for the preload values $\delta = 0.45$ and 0.5 in both directions. By increasing the preload value to $\delta = 0.55$, the frequency responses of the rotor center become quasi-periodic motion and this behavior persists at $\delta = 0.6$.

In Figure 15, a qualitatively different behavior can be observed in the range of $0.4 \leq \delta \leq 0.602$. Local bifurcation of the rotor center in the preload range of $0.51 \leq \delta \leq 0.602$ is shown in Figure 16. The results show that, before $\delta = 0.522$, the system has a periodic motion in the horizontal and vertical directions. Figures 17(a) and (b) show the Poincare maps at $\delta = 0.45$ and 0.5, respectively. One point on these maps confirms the T-periodic motion of the rotor in both displacements. It can be seen that quasi-periodic motion occurs in the interval of $0.522 \leq \delta < 0.602$. The Poincare maps at $\delta = 0.55$ and o.6 are shown in Figures 17(c) and (d) and the closed curve formed on this map demonstrates quasi-periodic motion of the rotor center at these values. When preload value exceeds $\delta = 0.602$, contact between rotor and bearing would occur.

CONCLUSION

The effect of preload on nonlinear dynamic behavior of a rigid rotor supported by two-lobe noncircular aerodynamic journal bearings has been studied in this study. Due to the nonlinearity of the gas film force, computational methods have been employed to study the dynamical behavior of the system. Dynamical

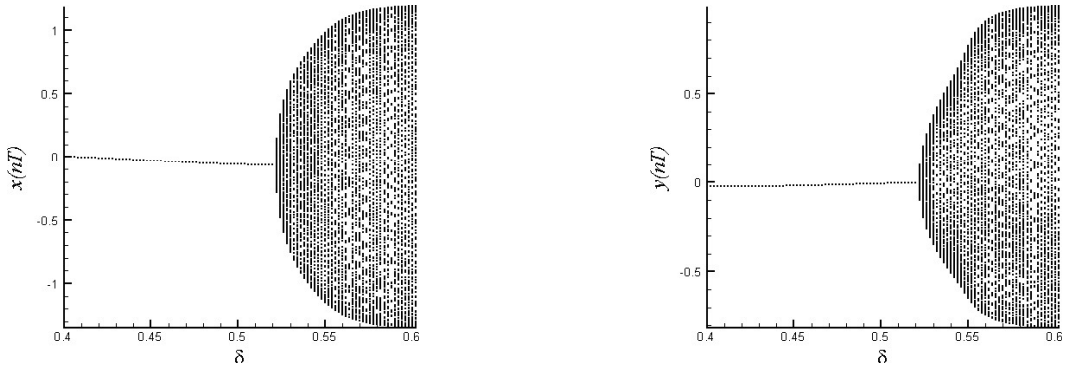

Figure 15. Bifurcation diagrams: (a) $x(nT)$ and (b) $y(nT)$ versus preload for $\lambda = 1.5$.

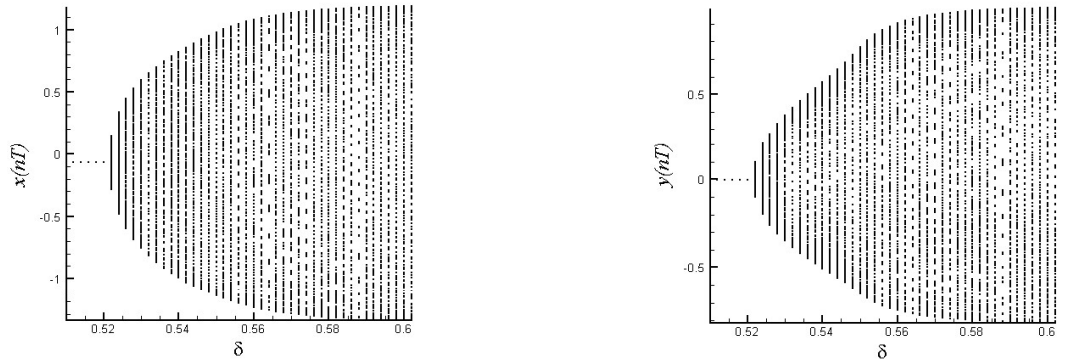

Figure 16. Local bifurcation diagrams of (a) $x(nT)$ and (b) $y(nT)$ versus preload $(0.51 \leq \delta \leq 0.602)$ for $\lambda = 1.5$.

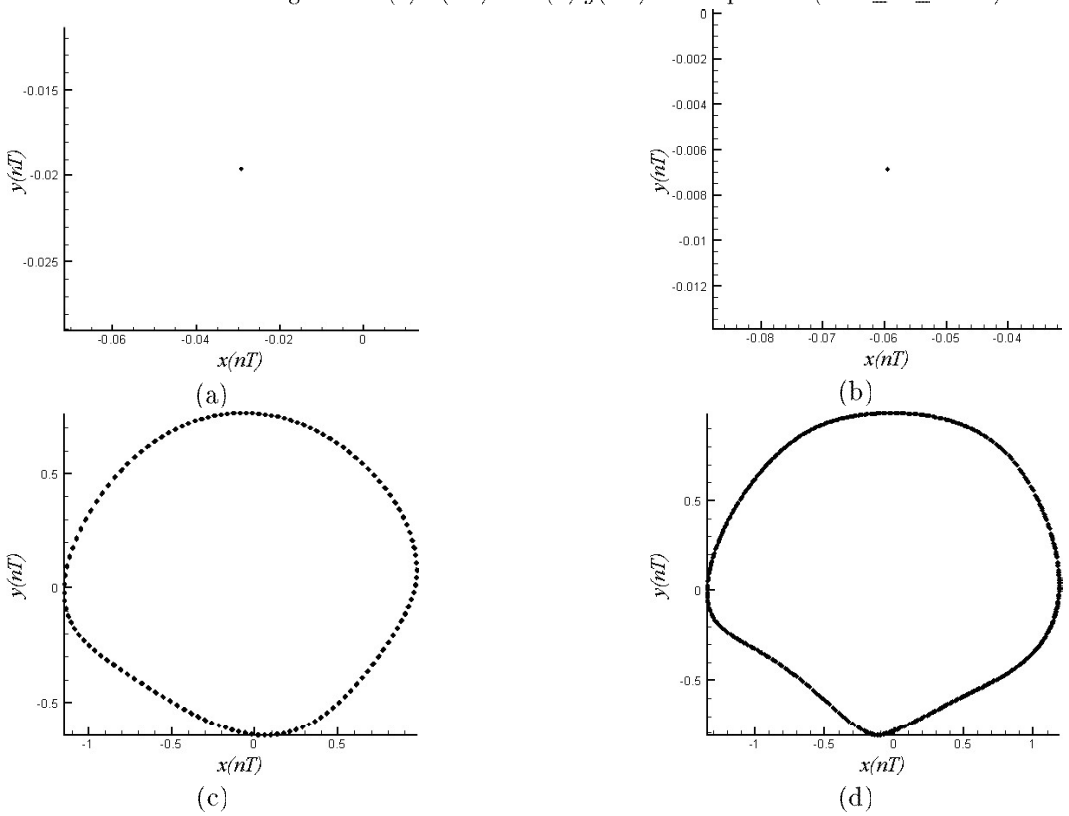

Figure 17. Poincare maps of the rotor center trajectory at (a) $\delta = 0.45$, (b) 0.5, (c) 0.55, (d) 0.6.

orbits, power spectra, Poincare maps and bifurcation diagrams are used to identify the dynamic behavior of this system.

From this study, it is shown that by considering the preload value as a parameter of the system, periodic, KT-periodic, quasi-periodic motions as well as contact between rotor and bearing occur in eccentric two-lobe bearings. It is found that at lower preload values, the system has better stability in a dynamical state. Also, by increasing the bearing aspect ratio, the onset of quasi-periodic motion and the contact between rotor and bearing occur at higher values of preload.

The variation of this parameter plays a major role in noncircular bearing systems. Thus, by changing the system parameter to suitable values, rotor center can be avoided from the undesirable behavior.

REFERENCES

1. Castelli, V. and Elrod, H.G., "Solution of the stability problem for 360 degree self–acting, gas–lubricated bearing", *ASME Journal of Basic Engineering*, **87**, PP 199-212(1961).
2. Ausman, J.S., "Linearized PH stability theory for translatory half-speed whirl of long self-acting gas-lubricated journal bearings", *ASME Journal of Basic Engineering*, **83**, PP 611-619(1963).
3. Holmes, A.G., Ettles, C.M. and Mayes, I.W., "The aperiodic behavior of a rigid shaft in short journal bearings", *International Journal for Numerical Methods in Engineering*, **12**(4), PP 695-702(1978).
4. Chandra, M., Malik, M. and Sinhasan, R., "Comparative study of four gas-lubricated noncircular journal bearing configuration", *Tribology International*, **16**(2), PP 103-108(1983).
5. Zhao, J.K., Linnentt, I.W. and Melean, L.J., "Subharmonic and quasi-periodic motion of an eccentric squeeze film damper-mounted rigid rotor", *ASME Journal of Vibration and Acoustic*, **116**(3), PP 357-363(1994).
6. Adiletta, G., Guido, A.R. and Rossi, C., "Chaotic motion of a rigid rotor in short journal bearings", *Nonlinear Dynamics*, **10**(3), PP 251-269(1996).
7. Adiletta, G., Guido, A.R. and Rossi, C., "Nonlinear dynamics of rigid unbalanced rotor in short bearings Part I: Theoretical Analysis", *Nonlinear Dynamics*, **14**(1), PP 57-87(1997).
8. Adiletta, G., Guido, A.R. and Rossi, C., "Nonlinear dynamics of rigid unbalanced rotor in short bearings Part II: Experimental Analysis", *Nonlinear Dynamics*, **14**(2), PP 157-189(1997).
9. Czolczynski, K. and Kapitaniak, T., "Hopf bifurcation in rotors supported in gas bearings", *Chaos, Solitons & Fractals*, **8**(4), PP 499-515(1997).
10. Wang, C.C. and Chen, C.K., "Bifurcation analysis of self-acting gas journal bearings", *Journal of Tribilcgy*, **123**(4), PP 755-767(2001).
11. Wang, C.C., Jang, M.J. and Chen, C.K., "Nonlinear dynamic analysis of a flexible rotor supported by self-acting gas journal bearing", *Proceedings of the Instruction of Mechanical Engineering*, **218**(12), PP 1527-1538(2004).
12. Wang, J.S. and Wang, C.C., "Nonlinear dynamic and bifurcation analysis of short aerodynamic journal bearings", *Tribology International*, **38**(8), PP 740-748(2005).
13. Wang, C.C., "Nonlinear dynamic behavior and bifurcation analysis of a rigid rotor supported by relatively short externally pressurized porous gas journal bearing system", *Acta Mechanica*, **183**(1), PP 41-60(2006).
14. Wang, C.C., "Bifurcation analysis of an aerodynamic journal bearing system considering the effect of stationary herringbone grooves", *Chaos, Solitons & Fractal*, **33**(5), PP 1532-1545(2007).
15. Wang, C.C., Yau, H.T., Jang, M.J. and Yeh, Y.L., "Theoretical analysis of the non-linear behavior of a flexible rotor supported by herringbone grooved gas journal bearings", *Tribology International*, **40**(3), PP 533-541(2007).
16. Wang C.C., "Theoretical and nonlinear behavior analysis of a flexible rotor supported by a relative short herringbone-grooved gas journal-bearing system", *Physica D-Nonlinear Phenomena*, **237**(18), PP 2282-2295(2008).
17. Wang, C.C. and Yau, H.T., "Application of a numerical method to the bifurcation analysis of a rigid rotor supported by a spherical gas journal bearing system", *Nonlinear Dynamic*, **51**(4), PP 515-528(2008).
18. Wang C.C., "Application of a hybrid method to the nonlinear dynamic analysis of a flexible rotor supported by a spherical gas-lubricated bearing system", *Nonlinear Analysis*, **70**(5), PP 2035-2053(2009).
19. Rahmatabadi, A.D. and Rashidi, R., "Effect of mount angle on static and dynamic characteristics of gas-lubricated, noncircular journal bearings", *Iranian Journal of Science and Technology*, **37**(B3), PP 27-37(2006).
20. Rahmatabadi, A.D. and Rashidi, R., "Investigation of preload effects on noncircular gas bearing systems performance", *Journal of Aerospace Science and Technology*, **4**(1), PP 33-38(2007).